Undulator linear taper control at the European X-Ray Free-Electron Laser facility

Sergey Tomin,* Jan Kaiser, Nils Maris Lockmann, Torsten Wohlenberg, and Igor Zagorodnov

Deutsches Elektronen-Synchrotron DESY, Notkestraße 85, 22607 Hamburg, Germany

(Received 17 July 2023; accepted 6 March 2024; published 12 April 2024)

Undulator tapering controls the resonance properties of the free-electron laser (FEL) amplification process. Wakefield energy losses in an undulator's vacuum chamber are one of the factors that determine the undulator's linear taper. While another contribution to energy losses, namely the losses due to spontaneous radiation, can be calculated analytically, estimating wakefield energy losses requires detailed knowledge of the chamber geometry and the electron beam current profile. We introduce a method for the automatic estimation of wakefield energy losses, which leverages noninvasive THz diagnostics, a current profile reconstruction algorithm enhanced with machine learning, and a recently developed analytical wakefield function for the European XFEL's undulator beamline. The correctness of this method was validated by directly measuring wakefield-induced electron beam energy losses in the undulator section. This, in turn, enables the prediction of the optimal linear taper in the undulator.

DOI: 10.1103/PhysRevAccelBeams.27.042801

I. INTRODUCTION

Sustainable energy exchange between an electron beam and an electromagnetic (EM) wave with a wavelength λ occurs when the electromagnetic wave advances the electron beam by one radiation wavelength as the electron beam traverses one undulator period. This synchronism condition is achieved at the fundamental resonance wavelength:

$$\lambda = \frac{\lambda_u}{2\gamma^2}(1 + K^2/2), \tag{1}$$

where λ_u is the undulator period, γ is the electron energy in units of the rest of energy mc^2, and

$$K = \frac{eB_0\lambda_u}{2\pi mc} \tag{2}$$

is the dimensionless undulator deflection parameter with B_0 amplitude of the undulator magnetic field.

The energy transfer from the electron beam to the EM wave is not limitless and reaches saturation. This phenomenon accounts for the relatively low efficiency of a self-amplified spontaneous emission (SASE) FEL. For a uniform undulator in which K and λ_u remain constant, a SASE FEL reaches saturation at a power level of approximately $P_{\text{sat}} \approx \rho P_{\text{beam}}$, where P_{beam} is the electron beam power and ρ is the FEL efficiency parameter [1,2], known as the Pierce parameter [1], which is on the order of 10^{-3} for x-ray FELs.

To avoid or delay the saturation phenomena, the tapering was proposed, involving variations in the period or magnetic field (or both) along the axis [3,4]. This adjustment allows the tailoring of undulator characteristics to satisfy the synchronism condition over a wide range of electron energies. The effectiveness of undulator tapering for the postsaturation regime was first demonstrated in a 35 GHz microwave FEL amplifier [5].

Before saturation, in the exponential growth regime, the electron beam's energy losses due to FEL interaction are small and can be neglected [6]. However, in long undulator beamlines, such as the European XFEL [7], the energy losses due to spontaneous radiation emission and wakefields can be significant [6,8,9]. Figure 1 illustrates the average beam energy losses due to spontaneous radiation (SR) and wakefields for typical European XFEL (EuXFEL) parameters. For comparison, a 1-mJ SASE pulse energy corresponds to a 4-MeV energy loss on average for a 250-pC beam. Routinely, at the European XFEL, achieved SASE pulse energy is on the order of a few mJ.

To maintain the resonant condition Eq. (1) in the first part of the undulator before saturation, the undulator parameter K should decrease linearly with undulator distance z to compensate for the electron beam's energy losses due to SR and wakefields. After saturation ($z > L_{\text{sat}}$), K changes

*Corresponding author: sergey.tomin@desy.de

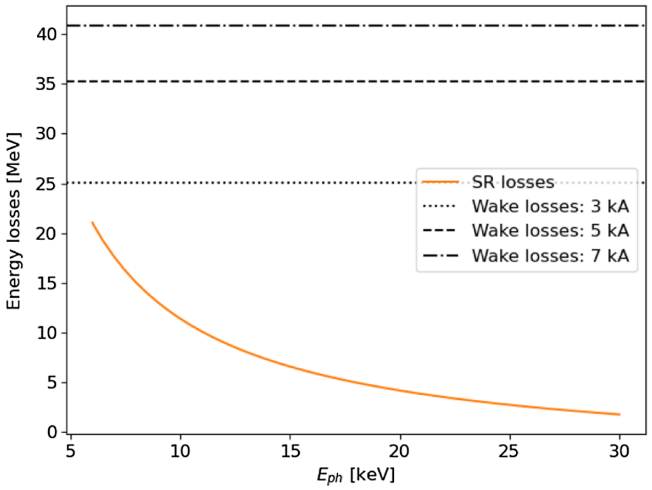

FIG. 1. Beam energy losses due to spontaneous radiation in SASE1 undulator (35 cells) as a function of undulator photon energy and wakefield energy losses of the beam core for Gaussian beams with amplitudes of 3, 5, and 7 kA. Electron beam energy 14 GeV.

nonlinearly to additionally compensate for energy losses due to the FEL interaction. The undulator taper formula employed at the European XFEL is as follows:

$$K(z) = K(0) - a \cdot z - b \cdot (z - L_{\mathrm{sat}})^c \cdot H(z - L_{\mathrm{sat}}). \tag{3}$$

Here a is a linear coefficient defined for SR and wakefields energy losses, while b and c are the coefficients defining nonlinear undulator taper. $H(\cdot)$ is the Heaviside function. These three coefficients are usually optimized manually during SASE tuning. In this work, we focus on the linear taper and how to predict coefficient a in Eq. (3).

The analytical formula for the energy losses of an electron beam in an undulator with length L and beam energy E due to spontaneous radiation is as follows:

$$U = \frac{4\pi^2}{3} \frac{r_e E^2 K^2 L}{mc^2 \lambda_u^2}. \tag{4}$$

where r_e is the classical radius of the electron. Calculating beam energy losses due to wakefields requires knowledge of both the impedance budget in the undulator beamline and the electron beam's current profile. To measure the current profile, we utilize an online noninvasive THz diagnostic called CRISP [10]. This diagnostic operates based on the coherent diffraction radiation generated as the electron beam passes through an open aperture in the screen. The resulting THz spectrum is then processed using a reconstruction algorithm [11] to obtain the electron beam's current profile. However, the CRISP reconstruction has a few limitations. One limitation is its inability to distinguish between the head and tail of the beam. In other words, the CRISP reconstruction can yield a flipped current profile, as it only measures the modulus of the Fourier transform of the current profile and not its phase [12]. The orientation of the current profile is important in the calculation of the wakefield potential, see Sec. III. Another limitation is of technical nature, as it is associated with limited temporal resolution when dealing with high peak currents and, conversely, a low signal-to-noise ratio for low current bunches [13]. These limitations can hinder the accurate estimation of wakefield losses of low and high beam current modes.

To overcome these limitations, we have developed a machine learning (ML) method that addresses and corrects the orientation issue of the reconstructed current profiles, while also providing higher temporal resolution. Furthermore, we have established an analytical wake function for the undulator beamline [14], which is used to calculate wakefield energy losses. To validate the estimation of wakefield energy losses, we conducted direct measurements. For precise measurement of beam energy changes on the order of tens of MeV in a 14 GeV beam, we utilized beam energy losses due to spontaneous radiation in the undulators to calibrate a beam energy monitor. The results of these direct measurements confirmed that our approach can accurately predict the total electron beam losses in the undulator, enabling the prediction of linear taper in the undulator.

The paper is organized as follows: First, the undulator beamline geometry and its analytical wake function are described in Sec. II. Second, a brief description of the THz diagnostic CRISP and the reconstruction current profile method enhanced with ML is provided in Sec. III. Third, the experimental validation of the wakefield energy losses calculation using a noninvasive diagnostic is presented in Sec. IV. Finally, the obtained results are discussed in Sec. V.

II. IMPEDANCE BUDGET OF THE UNDULATOR LINES

A. Impedance budget of the undulator cells

The European XFEL utilizes three long planar undulator lines: two hard x-ray undulators (SASE1/2) and one soft x-ray undulator (SASE3), Fig. 2. Each of these planar undulators consists of cells that adhere to a unified design. SASE1/2 contains 35 undulators with a period of 40 mm and SASE3 contains 21 undulators with a period of 68 mm.

The individual cell contains a 5-m long undulator and a 1.1-m intersection, which houses components, such as quadrupole, phase shifter, beam position monitor (BPM), and various vacuum components. In terms of wakefield calculation, we have a periodic structure with a period of $L_{\mathrm{cell}} = 6.1$ m. The vacuum chamber is identical across all cells. A detailed description of all the components of the undulator intersection, along with their contributions to the wakefield impedance, can be found in the Appendix.

An analytical approximation of the short-range longitudinal wake function of undulator periodic cells at the

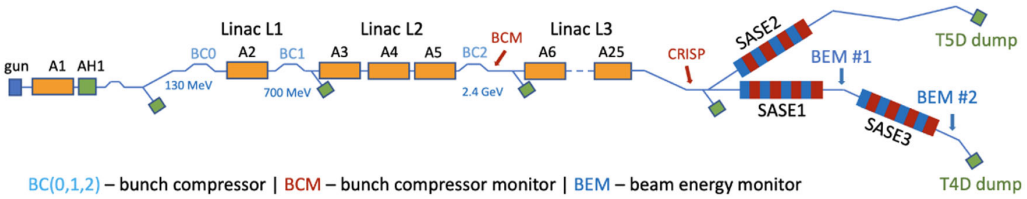

FIG. 2. Simplified layout of the European XFEL facility.

European x-ray free electron laser was obtained in [14]. From numerical and analytical calculations, the authors have found that the longitudinal wake function can be accurately approximated by the analytical expression

$$w_{\parallel}(s) = w_0(s) + \frac{\partial}{\partial s} w_1(s) + c\frac{R}{L}\delta(s), \tag{5}$$

$$w_0(s) = A\frac{Z_0 c}{\pi a^2}\exp\left(-\left(\frac{s}{s_0}\right)^{\alpha}\right)\cos\left(\frac{s}{s_1}\right), \tag{6}$$

$$w_1(s) = \frac{Z_0 c}{\pi^2 a L_{\mathrm{cell}}}\sqrt{2 g_0 s}, \tag{7}$$

where s is the distance between the source and the witness particles, Z_0 is free-space impedance, c is the velocity of light in vacuum, L_{cell} is the length of one undulator cell equal to 6.1 m, $A = 0.937$, $a = 5$ mm, $\alpha = 1.29$, $s_0 = 33.8\,\mu$m, $s_1 = 9.86\,\mu$m, $g_0 = 123$ mm, and $R = 30.5\,\Omega$. The parameters are obtained by a numerical fit of the parametric form of function w_0 to the direct sum of the wakes of different elements listed in Table II from the Appendix. The wake functions of each of these elements are described in [14]. Note that some of the coefficients are different from those published in [14] as we have corrected an error in the estimation of the wake of the round pipe in the intersection.

The longitudinal wake function $w_{\parallel}(s)$ describes the impact of the point charge alone. If the longitudinal wake function $w_{\parallel}(s)$ is known, then the longitudinal wake potential for an arbitrary linear charge density $\rho(s)$ can be found by convolution

$$W_{\parallel}(s) = -\frac{1}{Q}\int_{-\infty}^{s} w_{\parallel}(s-\eta)\rho(\eta)d\eta, \quad Q = \int_{-\infty}^{\infty}\rho(s)ds, \tag{8}$$

where Q is the electron bunch charge.

From the wake function, we estimate the loss factor $k_{\parallel}$ and the correlated energy spread $k_{\parallel,\mathrm{rms}}$:

$$k_{\parallel} = -\int_{-\infty}^{\infty} W_{\parallel}(s)\rho(s)ds,$$
$$k_{\parallel,\mathrm{rms}} = \left(\int_{-\infty}^{\infty}(W_{\parallel}(s) - k_{\parallel})^2\rho(s)ds\right)^{1/2}. \tag{9}$$

For a Gaussian bunch with a charge of 250 pC compressed to the peak current of 5 kA, the corrected impedance budget of one section with the contribution of all elements is shown in Table IV from the Appendix.

The wake functions of different components of the undulator lines are calculated separately and the total wake function is obtained as a direct sum of the individual contributions. However, for the bunches much shorter than the pipe radius, there must be significant impedance coupling between the components that are close to each other. Additionally, our estimation of the wake function uses the steady-state model of the resistive wakefield from [15] and neglects the transitive effect between the pipes with different materials. In [14], we have done a comparison of the used approach to the direct solution of Maxwell's equations in the time domain with a numerical code where the whole structure with all elements was simulated in one run.

In order to investigate these questions, we have created a rotationally symmetric model of the undulator vacuum chamber. The elliptical undulator pipe and other elements with the elliptical cross section listed in Table II from the Appendix have been replaced by round elements with an "equivalent" radius [14]

$$a = \frac{g}{\sqrt{F_{\parallel}^{\mathrm{ellip}}\left(\frac{g}{w}\right)}}, \tag{10}$$

$$F_{\parallel}^{\mathrm{ellip}}(x) = 0.279x^3 + 0.093x^2 + 0.013x + \pi^2/16, \quad g \le w, \tag{11}$$

where w is the half-width and g is the half-height of the elliptical cross section. We have neglected the roughness and the oxide layer effects. Additionally, we have considered only dc conductivity model. The pumping slots are replaced by round pipes of 5 mm radius. Let us note that the wake function given by Eq. (5) is obtained taking into account the roughness, the oxide layer, and the ac conductivity effects as they are important for our case of very short electron bunches [15].

For this "round" model, we have calculated the longitudinal wake function in the same way as described in the paper [14]. The energy losses $U(z)$ due to this model increase uniformly along the undulator section and its change $\Delta U(\Delta z)$ relative to the beginning of the undulator section can be written as

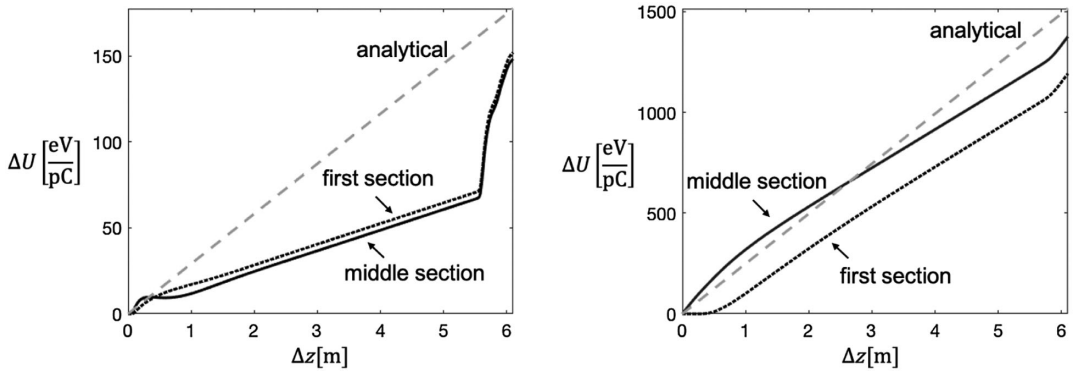

FIG. 3. Comparison of the analytical energy losses with the energy losses obtained from the numerical calculations with code ECHO for rotationally symmetric geometry. The left plot shows the results for the bunch length of 50 μm. The right plot shows the results for the bunch length of 10 μm. The solid black lines present the growth of the energy losses along one middle undulator section. The dotted black lines describe the energy losses that grow in the first undulator section. The gray dashed lines present the analytical energy losses.

$$\Delta U(\Delta z) = e k_{\parallel} \Delta z, \tag{12}$$

where Δz is the position in the undulator section relative to the beginning of the section, e is the charge of the electron, $k_{\parallel}$ is the "analytical" loss factor (per meter).

Alternatively, we have done direct numerical calculations with time-domain code ECHO [16]. Here we have started from the perfectly conducting pipe and considered three undulator sections with a total length of 18.3 m. The Gaussian bunch is traveling on the axis and we have calculated the energy losses of the bunch along the undulator line:

$$U(z) = -e \int_{-\infty}^{\infty} W_{\parallel}(s,z)\rho(s)ds,$$
$$W_{\parallel}(s,z) = -\frac{1}{Q}\int_{-\infty}^{z-s} E_z\left(z', t = \frac{z'+s}{c}\right)dz'. \tag{13}$$

The comparison of the analytical energy losses with the one obtained from the numerical calculations is shown in Fig. 3. The left plot shows the results for the rms bunch length σ of 50 μm. The solid black line presents the growth of the energy losses along one middle undulator section. The dotted black line describes the energy losses that grow in the first undulator section. The curves are different due to transitive effects at the beginning of the undulator line. The gray dashed curve presents the analytical energy losses. Similar results for the much shorter bunch length of 10 μm are shown in the right plot of Fig. 3.

If we define the "interference" factor $F_{\rm int}(\sigma)$ as a ratio of the numerical energy losses at the end of the middle section to the analytical energy losses of one section, then we can write $F_{\rm int}(50\ \mu{\rm m}) = 0.84$, $F_{\rm int}(10\ \mu{\rm m}) = 0.91$.

For the Gaussian bunch of length $\sigma = 10$ μm, the transient region in the pipe of radius $a = 5$ mm can be estimated as $a/(2\sigma^2) = 1.25$ m [17]. Indeed, we see in the right plot of Fig. 3 that the black solid curve demonstrates the steady-state behavior only after this distance from the beginning of the elliptical pipe. According to Table II from the Appendix, the elliptical pipe starts at 26 mm and ends at 5463 mm. It explains the behavior of the curves in the plot.

From the analysis of the transitive behavior, we can conclude that the analytical model, Eq. (5), could overestimate the total loss factor. However, for Gaussian bunches shorter than 10 μm, the overestimation is below 10%.

B. Wakefields of the experiment in undulator line SASE3

The measurement of the energy losses was done in the SASE3 undulator line between two beam energy monitors (BEMs) separated by 474 m as shown in Fig. 2.

The vacuum section between two BEMs consists of four main parts: (i) 23 standard undulator cells, (ii) chicane cells, (iii) 4 cells for the helical undulators, and (iv) round vacuum chamber of radius 20.25 mm with a length of 318 m, illustrated in Fig. 4.

In the chicane cell, the elliptical pipe is replaced by a flat pipe with an elliptical shape at one end and a round shape at

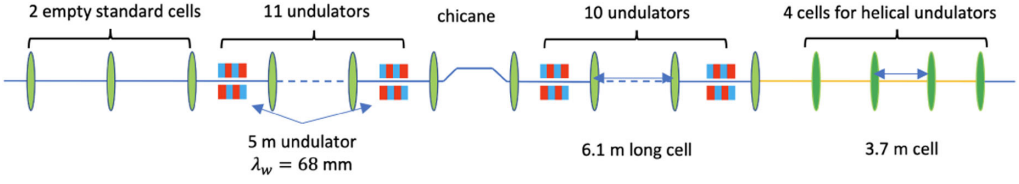

FIG. 4. SASE3 undulator line layout.

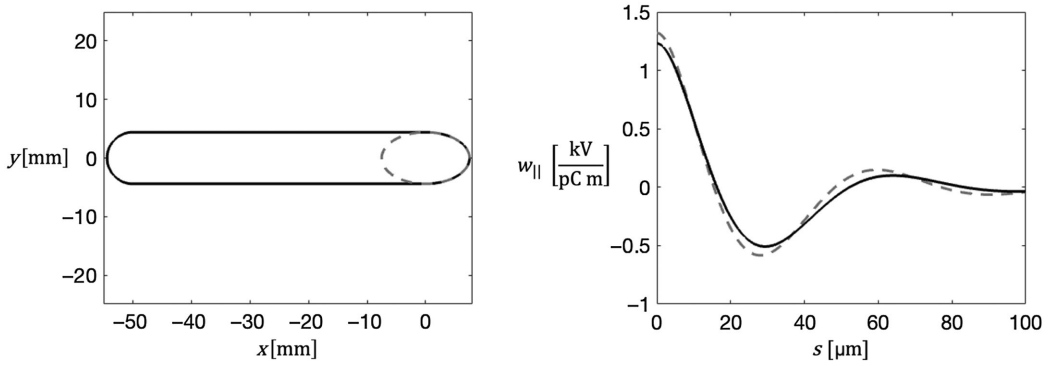

FIG. 5. Cross section of the chicane pipe (solid black line) and the undulator pipe (dashed gray line) are shown in the left plot. The right plot presents the longitudinal wake functions of the chicane pipe (solid black line) and the undulator pipe (dashed gray line) with the parameters of the aluminum from Table III.

another end as shown in the left plot of Fig. 5. The left plot of Fig. 5 compares the longitudinal wake functions of the chicane pipe and the undulator pipe at the position $(x, y) = (0, 0)$. The wake functions are obtained numerically with the boundary integral method described in [14]. We see that the bunches without deflection show approximately the same wakefields as in the standard undulator cell. Hence, we included this cell in the impedance budget as the standard undulator cell.

To estimate the wake function for the helical cells we followed the same approach as in [14]. The length of the intersection is 0.7 m. At the moment of the experiment in March 2021, the undulator pipe of 3 m was yet not installed and presented by standard stainless steel pipe of large radius of 20.25 mm. The contribution of several step-outs from radius of 5 mm to radius of 20.25 mm was estimated numerically by ECHO in order to take into account the transitive effects.

Let us define the total wake potential as

$$\hat{W}_{\parallel}(s) = eQ\hat{L}W_{\parallel}(s), \tag{14}$$

where $\hat{L}$ is the total length of the structure.

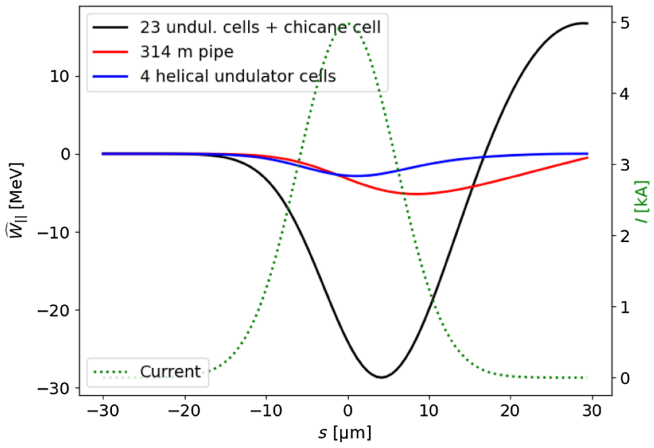

FIG. 6. Wakes of different parts for the Gaussian bunch with a length of 6 μm.

In order to show the relative contribution of these three main parts: (i) 23 standard undulator cells plus chicane cell, (ii) 4 cells for the helical undulators, and (3) a round vacuum chamber with a length of 318 m, to the total wake we considered a short Gaussian bunch with rms length of 6 μm and charge of 250 pC. Figure 6 shows the total wake potentials of the different parts. As expected, the main contribution is done by the undulator cells.

III. BEAM CURRENT PROFILE RECONSTRUCTION

Calculating beam energy losses due to wakefields requires knowledge of the electron beam's current profile. A direct measurement of the current profile in the time domain can be achieved using transverse deflecting structures (TDS). These structures facilitate the mapping of the longitudinal bunch distribution onto a transverse plane, enabling the observation and visualization of the current profile on a view screen [18]. However, measurements using TDS are invasive and constrained by the damage thresholds of view screens and the radiation limits for the emission of secondary particles. These limitations restrict the practicality and feasibility of conducting extensive or high-repetition-rate measurements using this method.

Another approach to obtaining information about the beam current profile is by observing the radiation emitted through the interaction of the beam with a medium, such as transition, diffraction, Smith-Purcell radiation, and others [19–25]. At the European XFEL, the current profile is monitored based on spectroscopy of coherent radiation. The coherent radiation spectrum and current profile of the electron bunch are linked via Fourier transform [26]. Coherent diffraction radiation (CDR) is generated by the electron bunch passing through an aperture inside an aluminum screen just upstream of the kicker-septum distribution system (see Fig. 2). While the electron bunches proceed undisturbed to the SASE beamlines, the THz and infrared spectrum of the CDR is detected by a multistage grating spectrometer CRISP [27]. CRISP at the European

XFEL is operated as a noninvasive current profile diagnostic at the megahertz electron bunch repetition rates [10].

Spectroscopic measurements are missing the phase function of the Fourier transform of the current profile that would be required for direct identification. Recently, iterative algorithms for phase retrieval in the one-dimensional case of longitudinal electron bunch reconstruction from spectroscopic data have been applied [28–30]. For CRISP diagnostics, the phase function is obtained through a combination of analytical and iterative phase retrieval methods, as described in [11]. This approach, referred to as CRISP reconstruction, has been demonstrated by comparative TDS measurements to perform excellently [10]. It is worth noting that, due to the missing phase function head and tail of the beam cannot be distinguished [12]. While this limitation does not pose a problem for operation or compression setups, it can impede the accurate estimation of wake losses in the lasing beam core if its position within the bunch is known.

To address this, we have developed a machine learning (ML) method to infer a correctly oriented current profile by incorporating two inputs: a 5-dimensional vector of rf settings $x_{\mathrm{rf}} = (\alpha, \rho, \psi, \alpha_{\mathrm{L1}}, \alpha_{\mathrm{L2}})$ and the 240-dimensional THz form factor vector x_{THz} sampled from the range of 0.7 to 58 THz [31]. The rf settings α, ρ, and ψ are translated to injector chirp, curvature, and skewness, while $\alpha_{\mathrm{L1}}, \alpha_{\mathrm{L2}}$ correspond to linac L1 and linac L2 chirps, respectively. The energy gain of the electron beam for these three stages is defined by design and can be found in Fig. 2. Both these inputs are concatenated and then passed through a multilayer perceptron neural network model, which then outputs 300 ordered samples of the current profile. The neural network (NN) is trained in a supervised setup to infer current profiles closely resembling those generated by a start-to-end beam dynamics simulation. The start-to-end beam dynamics simulations were performed using the OCELOT simulation code [32]. The tracking was conducted with 40k particles, including collective effects, following a similar approach as described in [33]. We conducted 32 000 simulations on the DESY high-performance cluster, randomly scanning rf parameters, which correspond to different beam compressions. From the current profiles obtained from the simulations, we generated CRISP form factors using the FFT algorithm and applied a CRISP spectrometer apparatus function that also models signal noise.

One of the difficulties in developing this neural network model is that the model must predict the current profile of bunches whose length can vary by a factor of 10 (Fig. 8), with acceptable resolution of the order of femtoseconds.

In order to cover a long bunch, the samples must be spread out over a wide range. In order to cover short bunches with adequate resolution, one must have a large number of samples. Not only does this needlessly increase the size of the neural network model, but it also means that a lot of the time, most of the neural network outputs are not predicting any useful information. This can lead to the model learning to output 0.0 on these simply because this is correct most of the time, instead of even attempting to learn the correct function for that particular sample.

We solve this problem by adding the bunch length $\hat{y}_s$ from the first to the last current sample as a second output of the neural network model. The 300 samples are then equidistantly arranged over the bunch length that the model inferred. This way, an adaptive resolution of the current profile $\hat{y}_I$ reconstructed by our model automatically reveals all relevant features, while also ensuring that the entire bunch is captured. The resulting neural network model $\mathcal{M}$ is given as

$$\hat{y}_I, \hat{y}_s = \mathcal{M}(x_{\mathrm{rf}}, x_{\mathrm{THz}}). \tag{15}$$

In between the input and the output layers, there are from two to six hidden layers, as is illustrated in Fig. 7. Each hidden layer may be followed by batch normalization

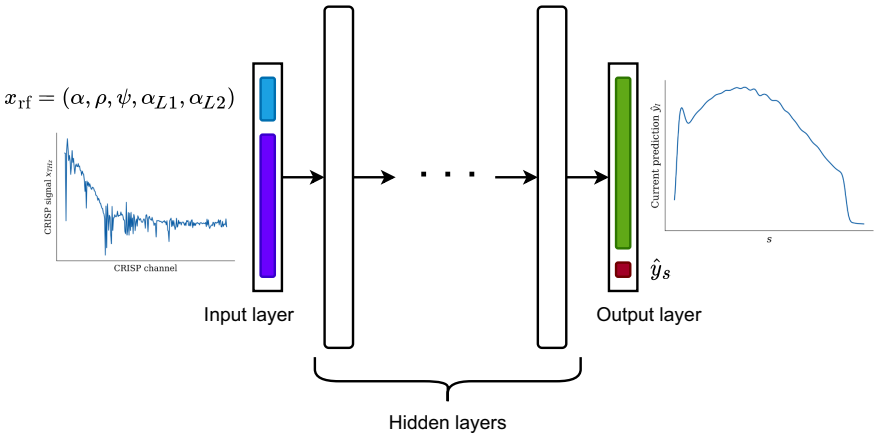

FIG. 7. Flowchart of the neural network architecture used for reconstructing the current profile. On the left side, the neural network receives input in the form of rf settings and THz spectrum. The signal is then passed through multiple hidden layers, and ultimately the current profile and bunch length are output on the right-hand side.

TABLE I. Hyperparameters used during training of the reconstruction model.

Parameter name	Value
Hidden layers	3
Hidden layer width	267
Hidden activation	ReLU
Batch normalization	Yes
Training epochs	76
Learning rate	0.003
Batch size	66

before the activation. The outputs use a different activation from hidden layers. Namely, a Softplus activation is chosen as the output activation function. The latter ensures that all outputs are strictly positive, as they physically should be, while also ensuring that there remains some gradient when the output should be zero according to the ground truth. If a rectified linear unit (ReLU) activation function were used on this output, gradients may be lost when 0 is output, which results in fully trained models that have single 0 samples where they stopped learning. We use a mean squared error (MSE) loss function L over each output where both outputs are weighted the same as in

$$L(y,\hat{y}) = \mathrm{MSE}(y_s,\hat{y}_s) + \mathrm{MSE}(y_I,\hat{y}_I), \tag{16}$$

with

$$\mathrm{MSE}(y,\hat{y}) = \frac{1}{n}\sum_{i=0}^{n}(y_i-\hat{y}_i)^2. \tag{17}$$

For training, an Adam [34] optimizer is used with $\beta_1 = 0.9$ and $\beta_2 = 0.999$. Hyperparameters, such as the number and width of hidden layers, or the learning rate was tuned using Bayesian optimization to minimize the loss over the validation dataset. The final used hyperparameters for one-dimensional current reconstruction are listed in Table I. The training dataset obtained from the simulations was randomly split into training, validation, and test sets according to the ratios (80%, 10%, and 10%). The rf settings and form factors are normalized over the training dataset to follow a standard normal distribution. Current profiles and bunch lengths are normalized to a range of (0,1).

In Fig. 8, four randomly selected examples are shown, each displaying the ground truth (current profile from the simulation dataset) as well as its reconstruction using the NN and CRISP methods. As can be seen, there is a good agreement between the ground truth and the profiles inferred by our neural network (NN) model in all four cases. In the case of the CRISP reconstruction, we observed that some of the current profiles are inverted, but the overall reconstructed current shape is in good agreement with the ground truth. It is worth noting that for samples A and D in Fig. 8, the CRISP reconstruction does not perform as well as the NN. In the case of high current, the time resolution of CRISP, which is about 8 fs [13], becomes a limiting factor, while for low current (<1 kA), the low signal level of CRISP limits the reconstruction performance.

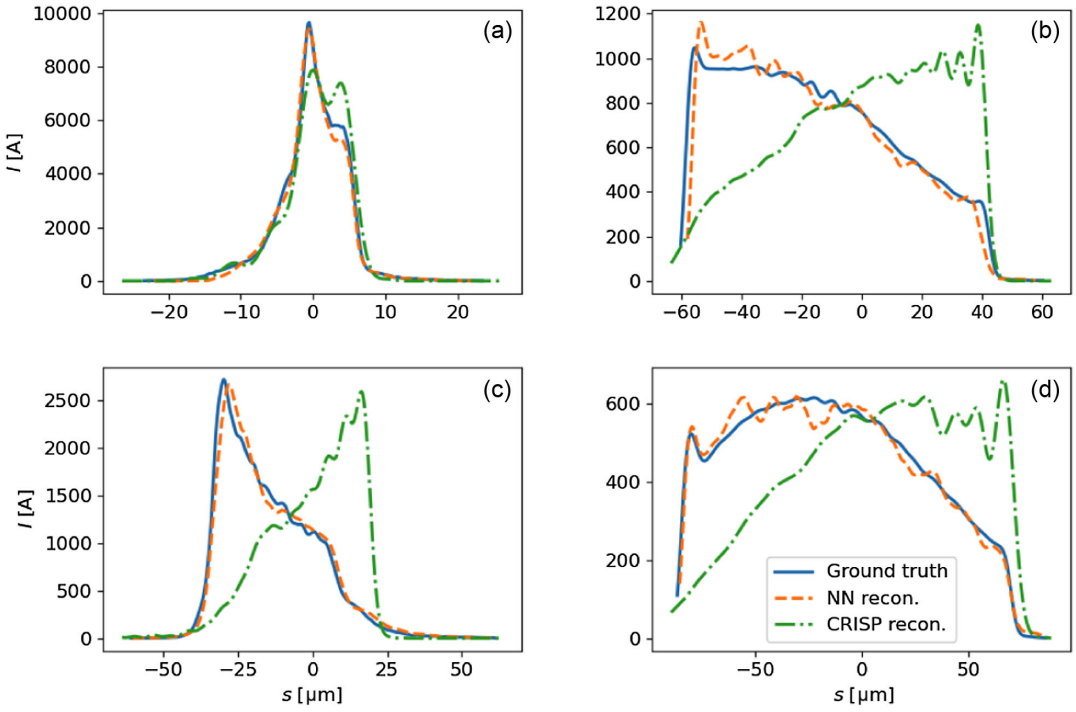

FIG. 8. Comparison of ground truth with the NN- and CRISP-reconstructed current profiles for random samples from the hold-out dataset.

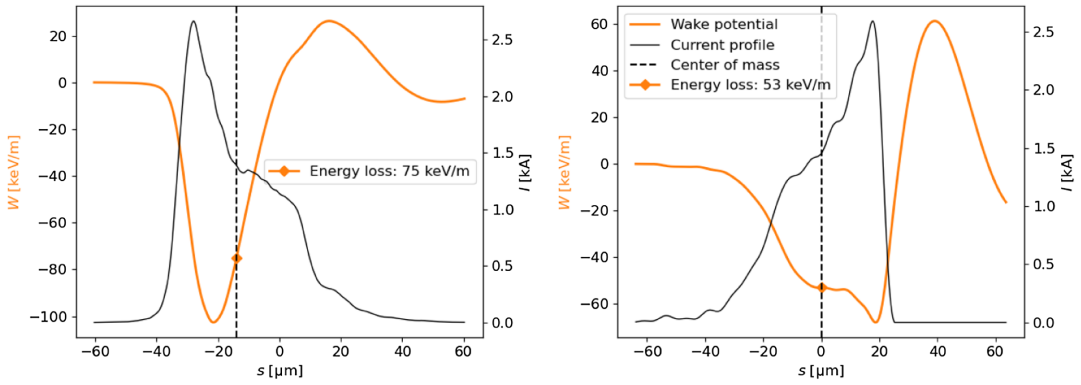

FIG. 9. Current profiles and wake potentials for the case Fig. 8(c). Left: NN reconstruction current profile and wake potential. Right: CRISP reconstruction and wake potential.

Let us examine Fig. 8(c) more closely and estimate average energy losses of the particle in the beam $eQk_{\|}$, also known as the loss factor, in the undulator vacuum chamber for the current profiles obtained with NN and CRISP reconstructions. The peculiarity of these profiles is that they are similar to each other but inverted.

The loss factor does not depend on the orientation of the current profile. This can be easily demonstrated by substituting one formula into another and changing the order of integration.

$$k_{\|} = \int_{-\infty}^{\infty}\int_{0}^{\infty} w_{\|}(\eta)\rho(s-\eta)\rho(s)d\eta ds = \int_{0}^{\infty} d\eta w_{\|}(\eta)\int_{-\infty}^{\infty}\rho(s)\rho(s-\eta)ds, \quad (18)$$

where $\int_{-\infty}^{\infty}\rho(s)\rho(s-\eta)ds$ is the autocorrelation function of the current profile, which exhibits symmetry.

The loss factor $eQk_{\|}$ for both cases, as expected, is similar and equal to approximately 48 keV/m. Now, let us assume that the position of the lasing slice corresponds to the center of mass of the beam. When we calculate the energy losses for the center of mass, we obtain different values. The NN reconstruction yields an energy loss of approximately 75 keV/m, whereas for CRISP reconstruction, it is 53 keV/m (see Fig. 9). However, if the lasing slice corresponds to the maximum current amplitude, the wakefield losses for both NN and CRISP reconstructions are similar, with values of approximately 73 and 68 keV/m, respectively.

IV. EXPERIMENTAL VALIDATION OF THE WAKEFIELD ENERGY LOSSES

Now that we have obtained the wake function for the undulator vacuum chamber and discussed a method for determining the beam current profile, we can estimate the beam energy losses due to wakefields and compare them with experimental measurements. Wakefield energy losses were measured in the SASE3 undulator line. The choice of the SASE undulator was motivated by two factors. First, it provided conveniently located diagnostics for electron beam energy measurements, known as the beam energy monitors (BEMs), as illustrated in Fig. 2. Second, the vacuum chamber between the BEMs is relatively simple, which facilitated the theoretical estimation of the impedance budget.

A. Calibration of the beam energy measurement diagnostics

Dispersion sections, equipped with beam position monitors (BPMs), are employed for absolute beam energy measurements along the accelerator. To enhance the reliability of beam energy measurements, readings from several consecutive BPMs are utilized, and trajectory fitting along these BPMs is applied to minimize reading noise. While this approach provides an acceptable accuracy for absolute energy measurements of about 1% [35], it may be less precise for small changes in the 10–20 MeV range caused by wakefield energy losses. For brevity, we refer to the entire system as a beam energy monitor (BEM). To overcome this limitation, we proposed a method for calibrating the BEM using the beam energy losses due to spontaneous emission. In Fig. 4, it can be seen that SASE3 comprised 21 undulators, each 5-m long with a period of 68 mm. These undulators were sequentially closed in groups of three cells to a minimum gap corresponding to the photon energy 660 eV at a beam energy of 14.1 GeV. The resulting beam energy changes were recorded by BEM 2, as shown in Fig. 10. The theoretical prediction given by Eq. (4) is also displayed in the figure, indicating that the raw measurements of BEM 2 overestimate the actual losses by a factor of 1.99/1.28. A similar technique was recently employed in [36], demonstrating good agreement with direct measurements.

As explained in the next section, wakefield energy loss measurements were conducted for various current profiles, or in other words, at different beam compression settings.

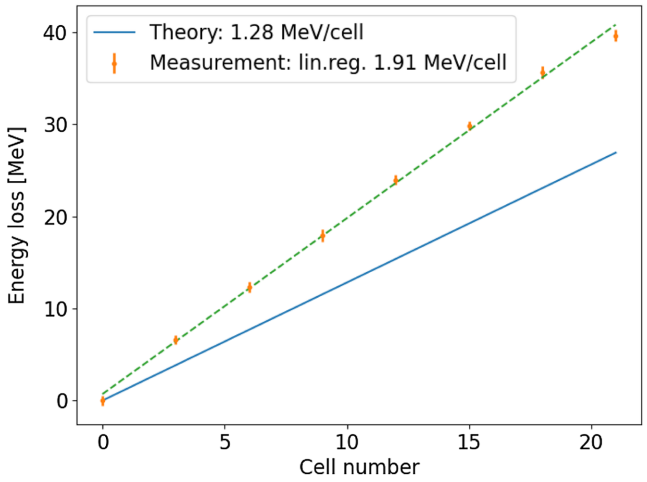

FIG. 10. Measurements of the energy losses due to spontaneous radiation and linear regression of the measurement points. Blue line is energy losses according to theoretical prediction.

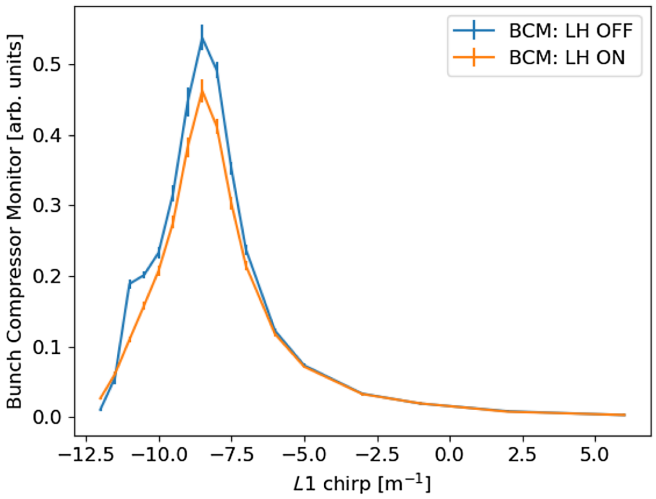

FIG. 11. Signal from bunch compressor monitor after the last bunch compressor BC2 during two beam compression scans, with laser heater on and off. A higher BCM signal corresponds to a greater amplitude of the beam current.

During a compression scan, it is reasonable to expect changes in beam energy at the BEM 1 position to occur due to wakefield loses in the vacuum chamber of the accelerator section from the L1 linac to BEM 1. Rather than applying the same calibration procedure to the first BEM, we maintained a constant beam energy throughout the entire experiment at this position (BEM 1), using energy feedback based on the last rf station A25. This approach simplifies the experiment.

B. Measurements results

The experiment was conducted as follows. We scanned the linac L1 chirp from $+6$ to -12 m^{-1}. The chirp is defined as $\frac{-ekV\sin\phi}{E_0+eV\cos\phi}$, where V and ϕ are the voltage and the phase of linac L1, $E_0 = 130$ MeV is the initial energy of the beam before L1, and $k = 2\pi f/c$, $f = 1.3$ GHz. Such a wide range was chosen to pass through the full compression. The chirp scan started at $+6$ m^{-1}, which corresponds to low compression and, accordingly, low beam current amplitude. As the chirp changed toward negative values, the beam compression increased, reaching a maximum at a chirp value of -8.5 m^{-1}. After passing the full beam compression, the overcompression phase occurred, and the amplitude of the beam current began to decrease. The scanning step was chosen to be nonuniform, with a denser grid around the region of full compression. The scan was carried out twice, with the laser heater [37] turned off and on. The laser heater introduces an uncorrelated energy spread, which results in a reduced current amplitude at full compression. The laser heater's intensity was selected to be near its maximum capacity, ensuring that its impact would be clearly visible. The final beam compression was also independently monitored by the beam compression monitor (BCM) [38] after the last bunch compressor BC2 (Fig. 11).

At each scanning step, we acquired the coherent diffraction radiation spectrum of the electron beam using CRISP for subsequent beam current profile reconstruction. We measured the energy loss of the entire bunch, also known as the loss factor, which depends solely on the shape of the current profile and not on its orientation. In this particular case, we utilized CRISP reconstruction as not all rf parameters for NN reconstruction were reliably recorded during the time of the experiment in March 2021.

The measurement of the beam energy loss due to wakefields was carried out using BEM 2 and a previously measured calibration coefficient $C = 0.64$. As mentioned earlier, the electron beam energy at the BEM 1 position remained constant due to energy feedback.

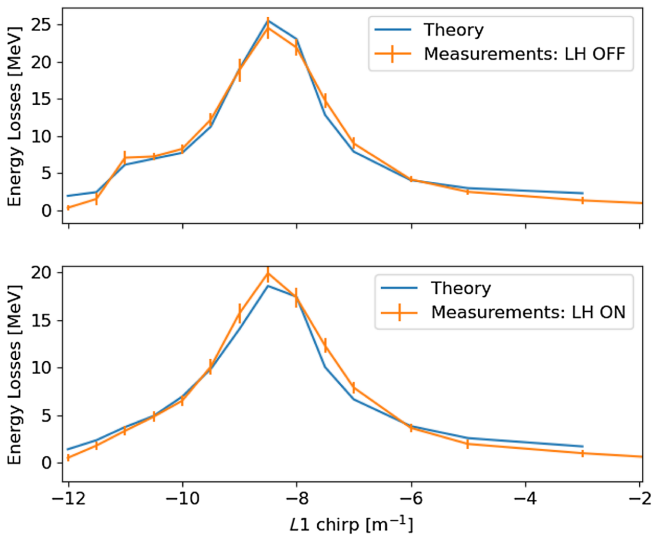

FIG. 12. Comparison between direct measurements of the energy losses and analytical estimations.

These measurements of beam energy losses are relative. We estimated the wakefield energy losses in the range of 0.3–0.4 MeV at the lowest compression (chirp $= 6$ m^{-1}). This assumption was made based on the estimation that the current profile amplitude was on the order of 0.1 kA at this compression point. However, CRISP cannot reliably reconstruct current profiles below 1 kA due to a low signal-to-noise ratio, as mentioned earlier. As a result, only a portion of the scan, specifically from -12 to -2.5 m^{-1}, can be utilized for the analytical estimation of wakefield energy losses. The final results, as depicted in Fig. 12, demonstrate a reasonable agreement between the analytical estimation and direct measurements of the wakefield-induced beam energy losses.

V. DISCUSSION AND SUMMARY

In the exponential growth regime, the total beam energy losses in undulators are mainly defined by wakefields and spontaneous radiation emission. These two components determine the linear taper of the undulator. Spontaneous radiation energy losses can be calculated using the theoretical formula in Eq. (4) and do not require any special diagnostics. On the other hand, wakefield losses require knowledge of the wakefield impedance of the undulator vacuum chamber and the beam current profile.

In this work, we have demonstrated and experimentally validated that the available noninvasive diagnostic at the European XFEL, along with the estimated wake function of the undulator beamline vacuum chamber, are sufficient to predict wakefield energy losses with reasonable accuracy.

In the expression for the undulator taper given in Eq. (3), the coefficient a represents the linear taper. The coefficient a, the change of the parameter K per unit length can be calculated if the beam energy change $\delta\gamma$ is known. This calculation is achieved using the resonance condition, Eq. (1). After simple transformations and neglecting second-order terms $\delta\gamma$ and δK, we obtain

$$\frac{\delta K}{K} = \frac{1 + K^2/2}{K^2/2}\frac{\delta\gamma}{\gamma}. \tag{19}$$

An open question remains regarding how to define the lasing slice for a better estimation of the linear taper. One potential solution is the utilization of the recently installed corrugated structure intended for LPS diagnostics [39]. However, it should be noted that the LPS diagnostics is installed after the SASE2 undulator and cannot be used during photon delivery.

Additionally, we are looking forward to utilizing LPS virtual diagnostics [31,40] that can be used in the control room. By incorporating these advancements, we can automatically predict the linear taper, potentially enhancing lasing performance and reducing the dimensionality of the FEL tuning optimization problem. While this is still a question for the future, in the meantime, we propose compensating wakefield losses for the slice corresponding to the maximum amplitude of the current profile.

ACKNOWLEDGMENTS

The authors thank E. Schneidmiller and S. Walker for helpful discussions and corrections. We thank members of the European XFEL team for providing help and conditions to carry out the measurements.

APPENDIX: IMPEDANCE BUDGET OF UNDULATOR CELL

The individual undulator cell contains a 5-m long undulator and a 1.1-m intersection. The list of all the components that contribute to the wake potentials is shown in Table II. The layout of the undulator intersection is shown on Fig. 13. The properties of the materials used in the estimation of the steady-state resistive wall wakefields are presented in Table III.

For the Gaussian bunch with a charge of 250 pC compressed to the peak current of 5 kA, the impedance budget of one section with the contribution of all elements is shown in Table IV.

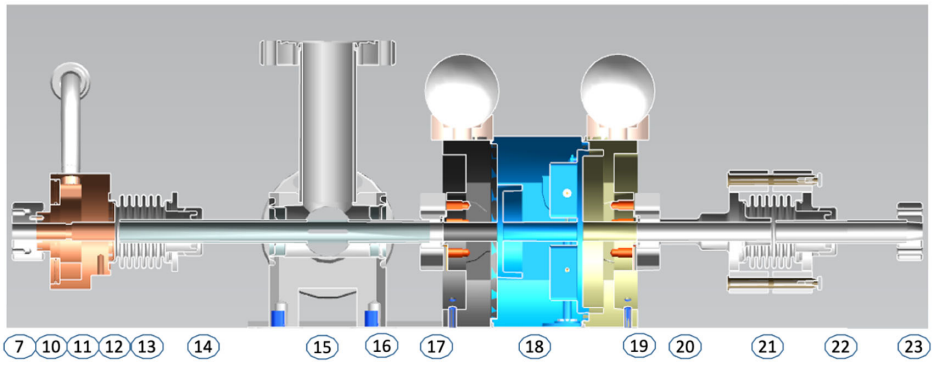

FIG. 13. Layout of the undulator intersection. The numbers under the elements correspond to the positions in Table II from the Appendix.

TABLE II. Components of the undulator lines along one section of the length of 6.1 m.

No.	Name	Half-width (mm)	Half-height (mm)	Position (mm)	Length (mm)	Material
1	Elliptical gasket	7.525	4.425	0	0.5	Silver
2	Flange, type I	7.5	4.4	0.5	13.0	Steel 316LN
3	Flange, type II	7.5	4.4	13.5	12.55	Aluminum
4	Weldseam	8.1	5	26.05	0.1	Steel 316LN
5	Elliptical pipe	7.5	4.4	26.15	5436.7	Aluminum
6	Weldseam	8.1	5	5462.85	0.1	Steel 316LN
7	Flange, type II	7.5	4.4	5462.95	12.55	Aluminum
8	Flange, type I	7.5	4.4	5475.5	13.0	Steel 316LN
9	Elliptical gasket	7.525	4.425	5488.5	0.5	Silver
10	Flange, type III	7.5	4.4	5489	27.5	Copper
11	Absorber	4.5	4	5516.5	3	Copper
12	Round pipe	5	⋯	5519.5	22.2	Copper
13	Below gap	12.75	⋯	5541.7	2.5	Copper
14	Round pipe	5	⋯	5544.2	96.3	Copper
15	Pumping slots	5	⋯	5640.5	21	Copper
16	Round pipe	5	⋯	5661.5	48.5	Copper
17	Round gasket	5.025	⋯	5710	0.5	Silver
18	BPM	5	⋯	5710.5	99	Steel 316LN
19	Round gasket	5.025	⋯	5809.5	0.5	Silver
20	Round pipe	5	⋯	5810	68.5	Cooper
21	Below gap	12.75	⋯	5878.5	2.5	Copper
22	Round pipe	5	⋯	5881	211	Copper
23	Round/elliptical transition	5–7	5–4.4	6092	8	Copper

TABLE III. Material properties.

Material	Conductivity $(\Omega m)^{-1}$	Relaxation time (fs)	Oxide layer (nm)	Roughness (nm)
Aluminum	3.66×10^7	7.1	5	300
Copper	5.8×10^7	24.6	5	300
Steel 316LN	1.4×10^6	2.4	0	300
Silver	6.2×10^7	40	0	300

TABLE IV. Impedance budget of one undulator section with length of 6.1 m for the Gaussian bunch with a charge of 250 pC compressed to the peak current of 5 kA.

No.	Name	Positions	Total length (mm)	Loss (kV)	Spread (kV)
1	Elliptical pipe	5	5426.7	584.0	275.5
2	Round pipe	12, 14, 16, 20, 22	446.5	49.5	24.0
3	Absorber	11	3.0	71.2	28.0
4	Round/elliptical transition	23	8.0	37.1	14.6
5	BPM	18	99.0	28.7	13.4
6	Below gaps	13, 21	5.0	12.0	4.8
7	Elliptical gaskets	1, 9	1.0	5.1	2.1
8	Round gaskets	17, 19	1.0	5.4	2.2
9	Pumping slots	15	21.0	5.3	2.2
10	Flanges, type I	2, 8	26.0	3.8	2.1
11	Flanges, type II	3, 7	25.1	2.7	1.3
12	Flange, type III	10	27.5	3.0	1.4
13	Weldseams	4, 6	0.2	2.3	0.9
	Totally		6100	811.4	352.5

[1] R. Bonifacio, C. Pellegrini, and L. Narducci, Collective instabilities and high-gain regime in a free electron laser, Opt. Commun. **50**, 373 (1984).

[2] C. Pellegrini, A. Marinelli, and S. Reiche, The physics of x-ray free-electron lasers, Rev. Mod. Phys. **88**, 015006 (2016).

[3] P. Sprangle, A. Ting, and C. M. Tang, Radiation focusing and guiding with application to the free electron laser, Phys. Rev. Lett. **59**, 202 (1987).

[4] N. M. Kroll, P. L. Morton, and M. N. Rosenbluth, Free-electron lasers with variable parameter wigglers, IEEE J. Quantum Electron. **17**, 1436 (1981).

[5] T. J. Orzechowski *et al.*, High-efficiency extraction of microwave radiation from a tapered-wiggler free-electron laser, Phys. Rev. Lett. **57**, 2172 (1986).

[6] W. M. Fawley, Zhirong Huang, Kwang-Je Kim, and Nikolai A. Vinokurov, Tapered undulators for SASE FELs, Nucl. Instrum. Methods Phys. Res., Sect. A **483**, 537 (2002).

[7] W. Decking *et al.*, A MHz-repetition-rate hard x-ray free-electron laser driven by a superconducting linear accelerator, Nat. Photonics **14**, 391 (2020).

[8] S. Reiche, Spontaneous radiation background calculation for LCLS, in *Proceedings of the 26th Free Electron Laser Conference, Trieste, Italy, 2004* (Comitato Conferenze Elettra, Trieste, Italy, 2004).

[9] D. Ratner *et al.*, FEL gain length and taper measurements at LCLS, in *Proceedings of the 31st International Free Electron Laser Conference, FEL-2009, Liverpool, UK* (STFC Daresbury Laboratory, Warrington, 2009).

[10] N. M. Lockmann, C. Gerth, B. Schmidt, and S. Wesch, Noninvasive THz spectroscopy for bunch current profile reconstructions at MHz repetition rates, Phys. Rev. Accel. Beams **23**, 112801 (2020).

[11] B. Schmidt, N. M. Lockmann, P. Schmüser, and S. Wesch, Benchmarking coherent radiation spectroscopy as a tool for high-resolution bunch shape reconstruction at free-electron lasers, Phys. Rev. Accel. Beams **23**, 062801 (2020).

[12] B. Schmidt, S. Wesch, T. Kövener, C. Behrens, E. Hass, S. Casalbuoni, and P. Schmuueser, Longitudinal bunch diagnostics using coherent transition radiation spectroscopy, arXiv:1803.00608.

[13] N. Lockmann, Noninvasive measurements of electron bunch current profiles with few-femtosecond resolution at MHz repetition rates, Ph.D. thesis, Verlag Deutsches Elektronen-Synchrotron, Hamburg, 2021.

[14] I. Zagorodnov, M. Dohlus, and T. Wohlenberg, Short-range longitudinal wake function of undulator lines at the European x-ray free electron laser, Nucl. Instrum. Methods Phys. Res., Sect. A **1043**, 167490 (2022).

[15] K. L. F. Bane and G. Stupakov, Resistive wall wakefield in the LCLS undulator beam pipe, Stanford Linear Accelerator Center, Stanford, CA, Technical Report No. SLAC-PUB 10707, 2004.

[16] I. Zagorodnov and T. Weiland, TE/TM field solver for particle beam simulations without numerical cherenkov radiation, Phys. Rev. ST Accel. Beams **8**, 042001 (2005).

[17] K. L. F. Bane, Wakefields of sub-picosecond bunches, Stanford Linear Accelerator Center, Stanford, CA, Technical Report No. SLAC-PUB-11829, 2006.

[18] P. Emma, J. Frisch, and P. Krejcik, A transverse rf deflecting structure for bunch length and phase diagnostic, Stanford Linear Accelerator Center, Stanford, CA, Technical Report No. TN-00-12, 2000.

[19] W. Barry, Measurement of subpicosecond bunch profiles using coherent transition radiation, AIP Conf. Proc. **390**, 173 (1997).

[20] M. Heigoldt, A. Popp, K. Khrennikov, J. Wenz, S. W. Chou, S. Karsch, S. I. Bajlekov, S. M. Hooker, and B. Schmidt, Temporal evolution of longitudinal bunch profile in a laser wakefield accelerator, Phys. Rev. ST Accel. Beams **18**, 121302 (2015).

[21] D. Mihalcea, C. L. Bohn, U. Happek, and P. Piot, Longitudinal electron bunch diagnostics using coherent transition radiation, Phys. Rev. ST Accel. Beams **9**, 082801 (2006).

[22] G. Doucas, M. F. Kimmitt, A. Doria, G. P. Gallerano, E. Giovenale, G. Messina, H. L. Andrews, and J. H. Brownell, Determination of longitudinal bunch shape by means of coherent Smith-Purcell radiation, Phys. Rev. ST Accel. Beams **5**, 072802 (2002).

[23] J. Thangara *et al.*, Demonstration of a real-time interferometer as a bunch-lenght monitor in a high-current electron beam accelerator, Rev. Sci. Instrum. **83**, 043302 (2012).

[24] A. Marinelli, M. Dunning, S. Weathersby, E. Hemsing, D. Xiang, G. Andonian, F. O'Shea, Jianwei Miao, C. Hast, and J. B. Rosenzweig, Single-shot coherent diffraction imaging of microbunched relativistic electron beams for free-electron laser applications, Phys. Rev. Lett. **110**, 094802 (2013).

[25] A. Curcio *et al.*, Noninvasive bunch length measurements exploiting Cherenkov diffraction radiation, Phys. Rev. Accel. Beams **23**, 022802 (2020).

[26] R. Lai, U. Happek, and A. J. Sievers, Measurement of the longitudinal asymmetry of a charged particle bunch from the coherent synchrotron or transition radiation spectrum, Phys. Rev. E **50**, R4294 (1994).

[27] S. Wesch, B. Schmidt, C. Behrens, H. Delsim-Hashemi, and P. Schmüser, A multi-channel THz and infrared spectrometer for femtosecond electron bunch diagnostics by single-shot spectroscopy of coherent radiation, Nucl. Instrum. Methods Phys. Res., Sect. A **665**, 40 (2011).

[28] S. I. Bajlekov, M. Heigoldt, A. Popp, J. Wenz, K. Khrennikov, S. Karsch, and S. M. Hooker, Longitudinal electron bunch profile reconstruction by performing phase retrieval on coherent transition radiation spectra, Phys. Rev. ST Accel. Beams **16**, 040701 (2013).

[29] D. Pelliccia and T. Sen, A two-step method for retrieving the longitudinal profile of an electron bunch from its coherent radiation, Nucl. Instrum. Methods Phys. Res., Sect. A **764**, 206 (2014).

[30] F. B. Taheri, I. V. Konoplev, G. Doucas, P. Baddoo, R. Bartolini, J. Cowley, and S. M. Hooker, Electron bunch profile reconstruction based on phase-constrained iterative algorithm, Phys. Rev. Accel. Beams **19**, 032801 (2016).

[31] J. Kaiser, A. Eichler, S. Tomin, and Z. Zhu, Machine learning for combined scalar and spectral longitudinal phase space reconstruction, in *Proceedings of the 14th International Particle Accelerator Conference, IPAC-2023, Venice, Italy* (JACoW, Geneva, Switzerland, 2023).

[32] S. Tomin, I. Agapov, M. Dohlus, and I. Zagorodnov, OCELOT as a framework for beam dynamics simulations of x-ray sources, in *Proceedings of the 8th International Particle Accelerator Conference, IPAC-2017, Copenhagen, Denmark* (JACoW, Geneva, Switzerland, 2017), WEPAB031.

[33] I. Zagorodnov, M. Dohlus, and S. Tomin, Accelerator beam dynamics at the European x-ray free electron laser. Phys. Rev. Accel. Beams **22**, 024401 (2019).

[34] D. P. Kingma and J. Ba, A method for stochastic optimization, arXiv:1412.6980.

[35] L. Froehlich (private communication).

[36] S. Tomin, E. Schneidmiller, and W. Decking, First measurement of energy diffusion in an electron beam due to quantum fluctuations in the undulator radiation, Sci. Rep. **13**, 1605 (2023).

[37] M. Hamberg, F. Brinker, and M. Scholz, Commissioning and first heating with the European XFEL laser heater, in *Proceedings of the 8th International Particle Accelerator Conference, IPAC-2017, Copenhagen, Denmark* (JACoW, Geneva, Switzerland, 2017), pp. 494–496.

[38] Ch. Gerth and N. M. Lockmann, Bunch compression monitor based on coherent diffraction radiation at European XFEL and FLASH, in *Proceedings of the 10th International Beam Instrumentation Conference, IBIC-2021, Pohang, Republic of Korea* (JACoW, Geneva, Switzerland, 2021).

[39] S. Tomin, W. Decking, N. Golubeva, A. Novokshonov, T. Wohlenberg, and I. Zagorodnov, Longitudinal phase space diagnostics with corrugated structure at the European XFEL, in *Proceedings of the 13th International Particle Accelerator Conference, IPAC-2022, Bangkok, Thailand* (JACoW, Geneva, Switzerland, 2022).

[40] J. Zhu, N. M. Lockmann, M. K. Czwalinna, and H. Schlarb, Mixed diagnostics for longitudinal properties of electron bunches in a free-electron laser, Front. Phys. **10**, 903559 (2022).